Influence of Carbide Morphology and Microstructure on the Kinetics of Superficial Decarburization of C-Mn Steels

HENRIQUE DUARTE ALVARENGA, TOM VAN DE PUTTE,
NELE VAN STEENBERGE, JILT SIETSMA, and HERMAN TERRYN

Decarburization is an important process during the heat treatment of steels. It can be divided into three separated events: dissolution of carbides, diffusion of carbon through the iron matrix, and surface reactions. The process is very sensitive to temperature. During intercritical annealing, austenite nucleates in the cementite-ferrite interface and grows at the rate determined by the diffusion of carbon in austenite. The presence of a decarburizing atmosphere during annealing guides the carbon diffusion in ferrite toward the surface, generating a flux of carbon from austenite toward ferrite, disturbing the austenite growth. In the presence of pearlite, the ferrite-austenite interface can be assumed to remain static until pearlite is completely dissolved, reducing then the carbon flux in austenite, consequently diminishing the austenite formation rate. At intercritical temperatures, the cementite-free ferrite layer at the surface reaches a greater width due to the combination of the thermodynamic fraction of austenite, dissolution rate of cementite, and the diffusivity of carbon in austenite and ferrite. In this study, an experimental investigation of the effects of the carbide morphology and distribution and the $\alpha - \gamma$ phase transformation in the decarburization kinetics on hypo-eutectoid steels is presented. It is suggested that the change of the dissolution kinetics of the carbides due to its morphology will affect the austenitization kinetics. Thus, the distribution of the carbon in the microstructure may determine the rate of decarburization in combination with the carbon diffusion through the phases or the gas-metal reactions.

DOI: 10.1007/s11661-014-2600-y
© The Minerals, Metals & Materials Society and ASM International 2014

I. INTRODUCTION

DECARBURIZATION is an important process during heat treatment of steels. It occurs at high temperatures in contact with substances that promote the oxidation of carbon, typically water vapor and hydrogen-containing atmospheres,[1,2] through the reactions, respectively:

$$C + H_2O \leftrightarrow CO + H_2 \quad [1]$$

$$C + 2H_2 \leftrightarrow CH_4 \quad [2]$$

HENRIQUE DUARTE ALVARENGA, Ph.D. Student, is with the Research Group Electrochemical and Surface Engineering (SURF), Vrije Universiteit Brussel, Pleinlaan 2, 1050 Brussels, Belgium, and also with the Department of Metallurgy and Materials Science, Universiteit Gent University, Technologiepark 903, 9052 Ghent, Belgium. Contact e-mail: hduartea@vub.ac.be TOM VAN DE PUTTE and NELE VAN STEENBERGE, Researchers, are with ArcelorMittal Global R&D Gent - OCAS, Pres. J.F. Kennedylaan 3, 9060 Zelzate, Belgium. JILT SIETSMA, Professor, is with the Department of Materials Science and Engineering, Delft University of Technology, Mekelweg 2, 2628 CD Delft, The Netherlands, and also with the Department of Metallurgy and Materials Science, Universiteit Gent University. HERMAN TERRYN, Professor, is with the Research Group Electrochemical and Surface Engineering (SURF), Vrije Universiteit Brussel, and also with the Department of Materials Science and Engineering, Delft University of Technology.

Manuscript submitted January 16, 2014.
Article published online October 8, 2014

Decarburization takes place during hot-rolling processes, especially in the production of springs, rods, and bars, and it changes the surface properties which may lead to failure of the component.[3,4] In other applications such as electrical steels and enameling, decarburization is intentionally induced during annealing in a reducing atmosphere, producing steel strip with very low-carbon concentration.[5–8] Because of its common occurrence, a good understanding of the mechanisms and the kinetics of decarburization is of essential importance, to improve quality and reduce costs of the processes.

For an initial microstructure that contains ferrite and carbides, and depending on the temperature, the physical mechanism that leads to decarburization is rather complex and can be divided into three different stages: dissolution of the carbides, the carbon diffusion through the ferrite and austenite phases, and the surface reaction. Surface reaction and carbon diffusion determine the decarburization width under atmospheres with low and high humidity, respectively.[7,9–15] The overall diffusion of carbon in steel depends on the phases present at given temperatures, as shown in Figure 1 for hypoeutectoid steels.

At a temperature above A_3 for pure iron, or 1185 K (912 °C), ferrite is not thermodynamically stable at low-carbon concentrations and the only phase present is austenite. In this case, the carbon can be assumed to be completely dissolved in austenite and the effect of the ferrite (α) to austenite (γ) transformation during decarburization can be ignored. Under this condition, the

decarburization mechanism can be described as a function of the diffusion of carbon in austenite,[4,12] as shown in Figure 1(a).

Below the intercritical region (i.e., below the A_1 temperature), the cementite dissolves directly into ferrite without the formation of austenite when the carbon is detracted from the material at the surface. Once in ferrite, carbon diffuses toward the surface, as illustrated in Figure 1(c). The region beneath the surface is characterized by the absence of carbides and is, therefore, referred to as ferrite layer.

At intercritical temperatures, cementite dissolves into austenite, which has greater carbon solubility than ferrite. The carbon diffuses through austenite to the $\alpha - \gamma$ interface, where it transfers to ferrite in which carbon diffuses rapidly toward the surface due to the gradient schematically shown in Figure 1(b). In this case, a ferrite layer forms beneath the surface. Its width is a function of time and it can be defined to extend from the surface to the dual phase region.[15,16] Some studies approached this case considering the presence of a moving interface similar to the description of the Stephan Problem.[17] These models simplify the microstructures by dividing it in two parts, the ferrite layer and a region with constant composition composed of a homogeneous mixture of ferrite plus austenite. Although this system considers the presence of the ferrite layer, it also implies that the carbides are instantaneous dissolved, and the carbon mobility in the dual phase region is limited only by the diffusion coefficient of carbon in austenite or ferrite. This assumption works reasonably well for materials with a composition close to the eutectoid due to the homogeneous presence of carbides throughout the matrix, which eases the determination of the ferrite layer.

The simplest method to investigate the decarburization depth is by measuring the micro-hardness as a function of the distance from the surface complementing it with examination of the ferrite layer by optical microscopy.[12,14,18] Although the effect of the presence of carbon on the micro-hardness is evident, its measurement does not unambiguously identify the presence of the ferrite layer. Instead, it measures the change in the mechanical properties caused by the change of carbon concentration and the density of carbides. Observation of the microstructure is a complementary technique due to the possibility to visualize the ferrite layer although the presence of carbides cannot always be quantified. A non-destructive method consisting of measurement of the magnetic hysteresis has also been used.[19]

In this work, low-carbon steels of the same composition but different carbide distribution and morphology were produced by lab-scale rolling. The kinetics of the austenite formation during annealing was investigated by Dilatometry, Field Emission Electron Probe Micro-Analysis coupled with Wavelength-Dispersive Spectroscopy (FE-EPMA-WDS), and Scanning Electron Microscopy (SEM). In addition, Glow Discharge Optical Emission Spectroscopy (GD-OES) was used to measure carbon concentration profiles as a function of the distance to the surface in steels annealed below, above and in the intercritical temperature region. A mechanism is discussed suggesting that in some cases carbide morphology and dissolution kinetics determine the rate of decarburization rather than the carbon diffusion through the phases or the gas-metal interface reactions, as is commonly accepted. This approach adds complexity to the previous models because the carbide dissolution occurs in different ways depending on the annealing temperature.

II. EXPERIMENTAL PROCEDURE

Steel sheets with a thickness of 25 mm, containing 0.12 wt pct carbon, and 0.2 wt pct manganese, were produced *via* a lab scale smelting.

The material was homogenized at 1523 K (1250 °C). The homogenization treatment is important to distribute the manganese evenly through the material. The manganese can have a small effect on carbide dissolution and on the kinetics of austenite-ferrite phase transformation due to partitioning effects. As the manganese concentration is small and within the limit of solubility in ferrite according to ThermoCalc Database,[20] this effect is assumed not to interfere significantly with the results obtained in this work. Quantitative analysis of the partitioning effect of manganese is beyond the scope of this work.

Subsequently, the material was hot rolled above the recrystallization temperature of austenite to a thickness of 3 mm followed by air cooling to its coiling temperature, as shown in Figure 2(a). Two different coiling temperatures were used: below, at 873 K (600 °C) and above the eutectoid temperature, at 1023 K (750 °C), which clearly leads to different carbide precipitation kinetics, generating different microstructures.

Steel sheets with a thickness of 25 mm, containing 0.12 wt pct carbon, and 0.2 wt pct manganese, were produced *via* a lab scale smelting. The material was homogenized at 1523 K (1250 °C) and subsequently hot rolled above the recrystallization temperature of austenite to a thickness of 3 mm, followed by air cooling to its coiling temperature, as shown in Figure 2(a). Two different coiling temperatures were used: below, at 873 K (600 °C) and above the eutectoid temperature, at 1023 K (750 °C), which clearly leads to different carbide precipitation kinetics, generating different microstructures. Slow cooling was performed in the furnace to simulate the effect of industrial coiling. The materials were then pickled to remove the superficial oxides and cold rolled to a final thickness of 1 mm. After cold rolling samples were machined to dimensions of $10 \times 5 \times 1$ mm^3 and used for dilatometry experiments.

The remaining material was cut to dimensions of $220 \times 120 \times 1$ mm^3 and used for decarburization annealing treatments in a reducing atmosphere consisting of 95 pct N_2, 5 pct H_2 with a dew point of 253 K (−20 °C) using a Reactive Annealing Process Simulator (RAPS).

After each rolling and annealing treatment, cross section samples were prepared following standard metallographic procedures. These were analyzed by optical microscopy and SEM. A Field Emission Microprobe (FE-EPMA) coupled with Wavelength Dispersive

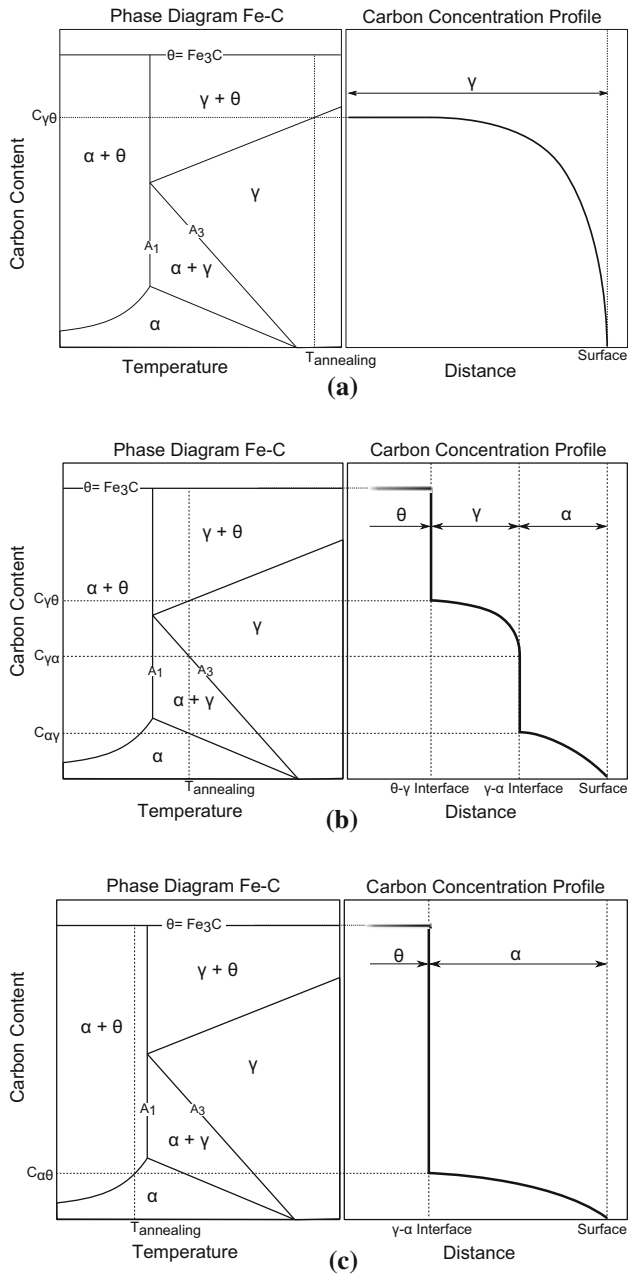

Fig. 1—Schematic carbon concentration profiles through the phases under a decarburizing atmosphere. The presence of the phases is determined by the concentration limits imposed by the Fe-C phase diagram (*a*) above the intercritical region, (*b*) in the intercritical region, and (*c*) below the intercritical region. The symbols α, γ and θ represents ferrite, austenite, and cementite, respectively.

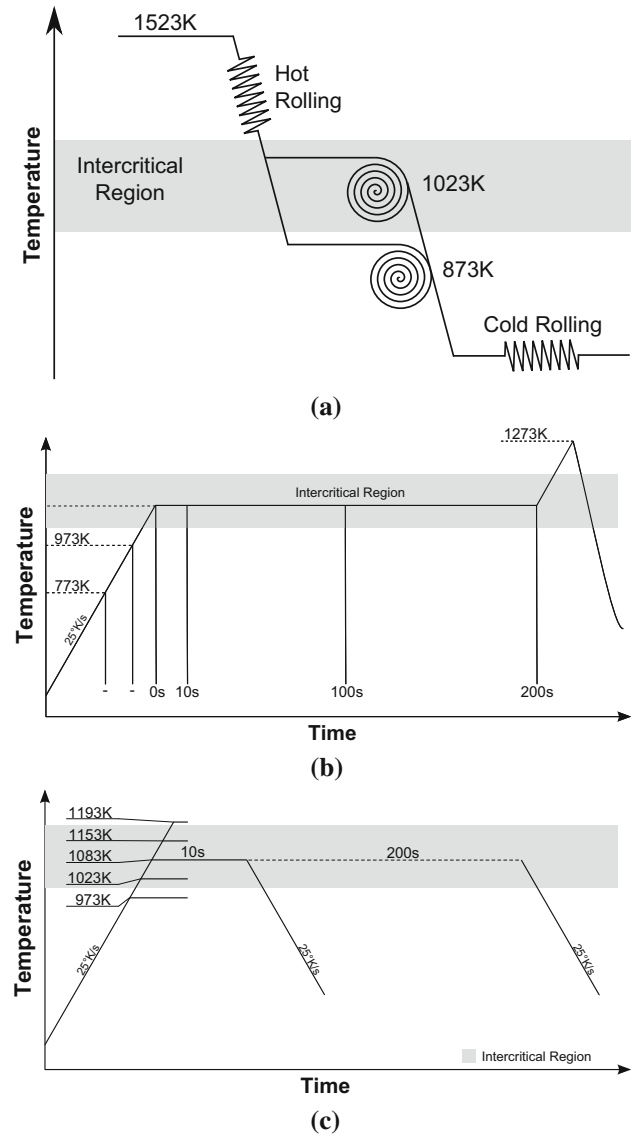

Fig. 2—Schematic representation of (*a*) the hot-rolling conditions: homogenizing temperature, hot rolling in the austenitic phase and coiling at 873 K and 1023 K (600 °C and 750 °C), (*b*) vacuum annealing at intercritical region quenched at different moments of the cycle by dilatometer simulator, and (*c*) decarburizing annealing cycles at different isothermal temperatures for 10 and 200 seconds performed in the RAPS simulator.

Spectrometers (WDS) JXA-8530F was used to map the carbon distribution and assess the microstructural features by the analysis of the carbon concentration.

Subsequently, dilatometry studies were performed to determine the initial and final temperature of phase transformation at constant heating rate of 25 K/s, which is common to all subsequent annealing cycles (Figures 2(b) and (c)). Isothermal treatments at intercritical temperatures were also performed in the dilatometer to evaluate the progress of the phase transformation during the isothermal holding. The same treatments were applied in the RAPS under decarburizing atmosphere. A subsequent heating to 1273 K (1000 °C) after isothermal annealing in the dilatometer was necessary to complete the austenitization and obtain kinetic data to correctly quantify the progress of the phase transformation. The volume fraction of austenite was obtained by the lever rule.[21]

Interrupted annealing cycles with quenching at different moments as shown on Figure 2(b) were performed in the dilatometer with the objective to study the evolution of the microstructure with the annealing.

For the decarburization studies, the samples were annealed according to the cycles shown in Figure 2(c). During the heating and isothermal steps an atmosphere of 95 pct N_2, 5 pct H_2 with a dew point of 253 K (−20 °C) was used. Cooling was performed under dry nitrogen atmosphere.

The isothermal temperatures were kept for 10 and 200 seconds at temperatures in the intercritical region at 1023 K, 1083 K, and 1153 K (750 °C, 810 °C, and 880 °C), above the intercritical region at 1193 K (920 °C) and below the intercritical region at 973 K (700 °C). The temperature of 973 K (700 °C) was also kept for 500 seconds.

Some decarburization already takes place during the homogenizing and hot-rolling steps, changing the carbon distribution in the vicinity of the surface. For a correct evaluation of the amount of carbon removed during annealing, the previous decarburization should also be taken into account. Therefore, carbon depth profiles by Glow Discharge Optical Emission Spectroscopy (GD-OES) were obtained before and after the decarburization annealing.

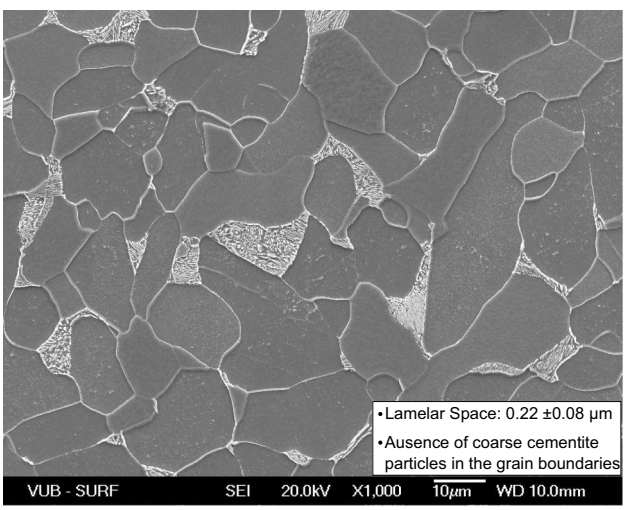

(a)

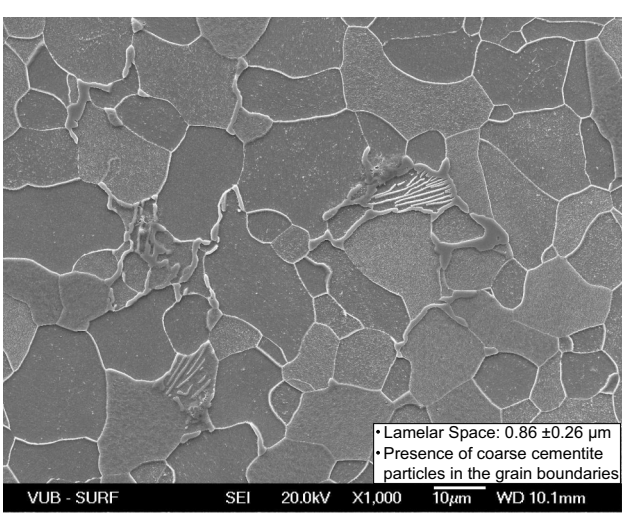

(b)

Fig. 3—SEM images of hot-rolled samples after coiling at (*a*) 873 K (600 °C) and (*b*) 1023 K (750 °C).

The GD-OES instrument used was a GDA-750 with discrete photo-multipliers (PMTs) for each spectral line of interest. A 4 mm anode was used covering an area of about 50 mm^2. The source conditions were set to 1000 V, 25 mA with variable pressure. The depth resolution is not greater than 1 μm. The main optical emission lines of interest were 156.144 nm for carbon, 249.318 nm for iron and 426.629 nm for argon.

Since the plasma occurs under an argon atmosphere, any change of the argon detection lines during the measurement indicates variations of the plasma conditions, which will have an effect on other detection lines. Because of this characteristic, the carbon intensity line was normalized by the argon line. This increases the stability of the signal and optimizes the quantification.[22,23] Another possible reference line is the iron intensity signal. Since iron is the major element of the samples, it also can be used as reference line. It will correct the carbon signal for variations existing in the structure of the samples but does not correct for the plasma variations.[24,25] Argon was, therefore, used as internal reference instead of iron because it shows better precision in the carbon calibration line in the lower concentration range.

The quantification was performed by the use of CRMs references. As the samples have similar matrices and the carbon concentration varies in a limited range from traces to 1200 ppm, the sputter rate and the emission yield can be considered constant.[23]

III. RESULTS AND DISCUSSION

A. *Initial Microstructure*

The coiling temperature is defined as the temperature at which the steel is coiled after hot rolling. It is an important processing parameter because after coiling the cooling rate is reduced dramatically due to heat transfer between the layers of the coil. Its change alters the kinetics of the phase transformations which will affect the interlamellar spacing of pearlite and the coarseness of cementite precipitates, and thus the carbon distribution.[26] At coiling temperatures below A_1, the eutectoid transformation occurs before the coiling and the cementite precipitates occur in the form of fine pearlite structures surrounded by a ferrite matrix, as seen in the microstructure after coiling at 873 K (600 °C) in Figure 3(a).

The increase of the coiling temperature coarsens the cementite. When the coiling temperature is above A_1 ferrite and austenite will coexist during the initial stage of coiling. The carbon concentrates in austenite due to its higher solubility. During cooling the fraction of ferrite increases, and the austenite becomes richer in carbon. The eutectoid transformation occurs at such a low cooling rate that very coarse pearlite is formed. Also cementite clusters precipitate at the grain boundaries instead of lamellar pearlite,[26,27] as shown in Figure 3(b). This type of transformation is called divorced eutectic transformation (DET).[28,29]

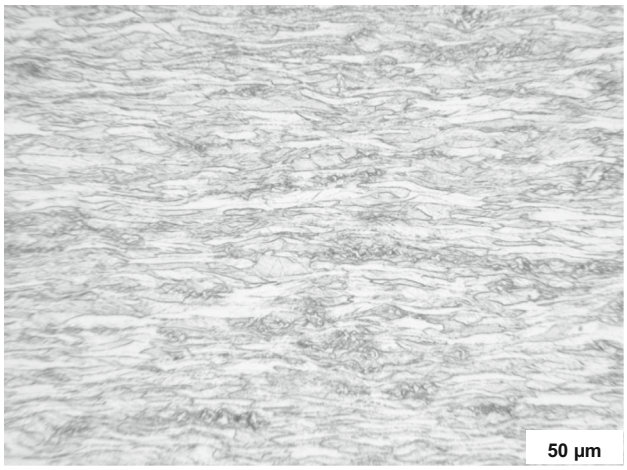

(a)

(b)

Fig. 4—Optical micrographs of the cold-rolled material heated at rate of 25 K/s following by quenching from (*a*) 773 K (500 °C) and (*b*) 973 K (700 °C), in a dilatometer.

B. *Dissolution of Carbides During Annealing*

To examine the microstructure evolution during annealing, cold-rolled samples coiled at 1023 K (750 °C) were used. Micrographs were taken after each annealing-quench cycle shown in Figure 2(b). The microstructure before annealing consists of typical cold-rolled structure of elongated ferrite grains and broken cementite as described by Van Cauter.[27] After heating until 773 K (500 °C) followed by quenching, no significant change in the microstructure is observed as shown in Figure 4(a), although recovery does take place. The sample submitted to interrupted heating at 973 K (700 °C) has a microstructure consisting of recrystallized equiaxial ferrite grains and broken cementite as shown in Figure 4(b).

Above the A_1 temperature, austenite nucleates preferentially at the interfaces between ferrite and cementite. The cementite will start to dissolve into newly formed austenite, which will grow around cementite. Seeing that the cementite present in the material coiled at 1023 K (750 °C) is very coarse and segregated, the austenite regions will also be coarsely distributed through the matrix. Figure 5 shows the progress of the austenite formation during isothermal holding at 1083 K (810 °C) for 200 seconds. The graph shows the fraction of austenite calculated from the dilatometric data as a function of time. The evolution of the austenitization is supported by the microstructural observations of the materials quenched at different moments of the annealing cycle. In the microstructure, the black regions are the martensite that was formed during quenching. Since the martensite is formed in a displacive transformation of austenite, its presence indicates the regions where austenite was present during annealing. In the beginning of the isothermal holding, 9 pct of austenite is already formed during heating.

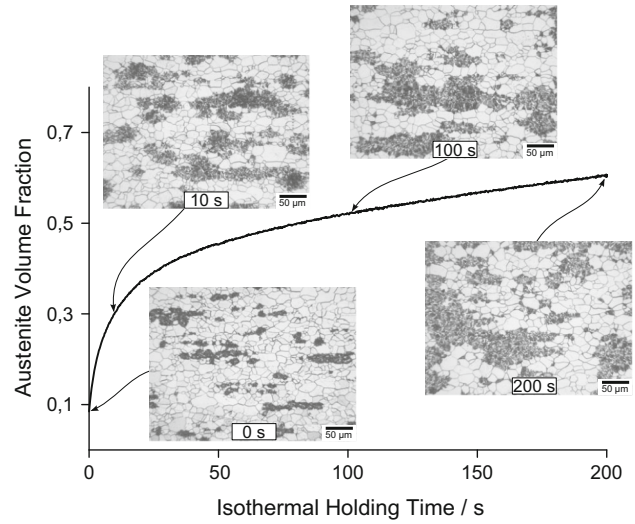

Fig. 5—Dilatometric results of the evolution of austenite fraction during isothermal annealing at 1083 K (810 °C) as a function with the holding time. The optical micrographs were obtained of samples quenched at different moments of the isothermal holding. Microstructure: ferrite + martensite. Etching: Nital 2 pct..

After the isothermal holding and cooling at 25 K/s, the austenite that had formed during the treatment is transformed into pearlite. The annealing treatment did not impact the microstructure significantly for materials submitted to a coiling temperature of 873 K (600 °C). Both before and after annealing the microstructure consists of ferrite and pearlite evenly distributed through the matrix as shown in Figure 3(a) and in Figure 6(a), respectively. As the carbides are evenly spread prior to the heat treatment, austenite grains nucleate uniformly during the heat treatment, subsequently re-transforming into pearlite, retaining the initial distribution pattern.

For materials coiled at 1023 K (750 °C) the situation is very different. The initial microstructure consists of relatively large pearlite colonies and large cementite particles, which have a lower surface-area density than fine pearlitic structures as observed in Figure 3. Consequently, the density of austenite nucleation sites is reduced dramatically, slowing down the austenite formation kinetics. Therefore, the austenite is formed in localized sites and grows around the slowly dissolving cementite particles. Finally, the austenite is transformed into fine pearlite during cooling at 25 K/s.

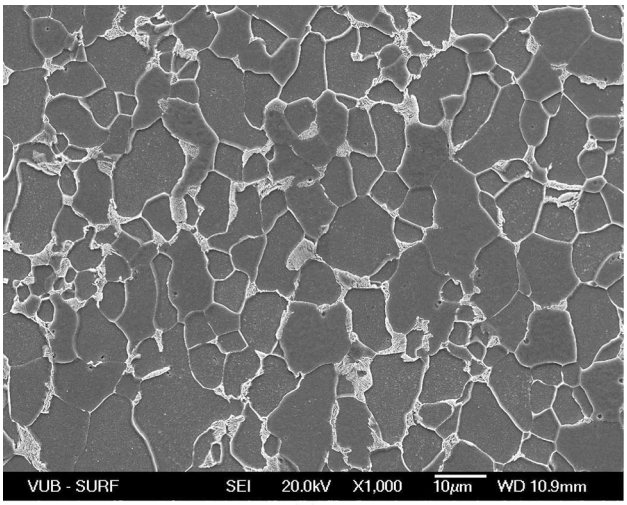

(a)

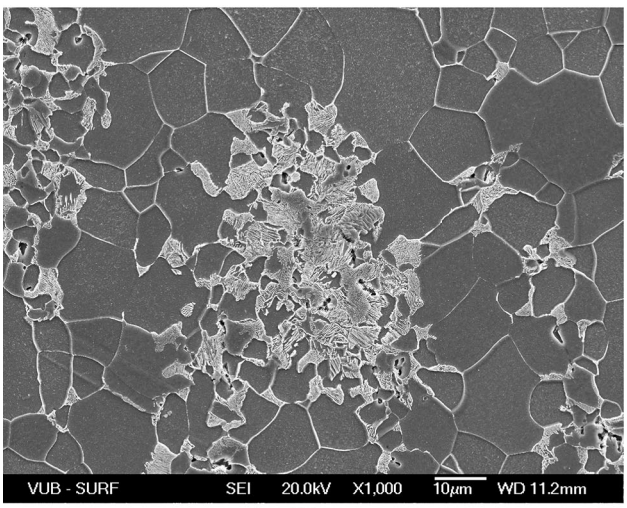

(b)

Fig. 6—SEM images of the final microstructure after annealing in a dry argon atmosphere at 1083 K (810 °C) for 200 s and a cooling rate of 25 K/s of samples coiled at (*a*) 873 K (600 °C) and (*b*) 1023 K (750 °C).

Figure 7 shows the evolution of the austenite fraction as a function of the temperature at a constant heating rate of 25 K/s. The results from two coiling temperatures are compared with the equilibrium fraction calculated *via* ThermoCalc.[20] It can be seen that in the material coiled at 873 K (600 °C), the phase transformation starts almost at the same temperature as the thermodynamic curve. The delay of the transformation is due to the heating rate. It can be noted in Figure 7 that the initial austenitization temperature for the material with coiling temperature of 1023 K (750 °C) is around 65 K higher than the thermodynamic temperature. As the heating rate is 25 K/s, the transformation starts 2.5 seconds later in comparison with the material of the low-coiling temperature.

In Figure 6(b) and in Figure 8(a) distinct feature is observed among the pearlite colonies: presumably a cementite particle that was partially dissolved during annealing. The qualitative analysis of the carbon distribution by means of FE-EPMA-WDS in Figure 8 shows that this particle is indeed rich in carbon. This structure is commonly found in material annealed just above the eutectic temperature, at 1023 K (750 °C) for 10 seconds. With the increase of the annealing temperature these distinct particles are less present, indicating their complete dissolution. Considering these facts and the morphological similarity with the cementite clusters prior to annealing, it is believed that this particle is indeed a partially dissolved cementite cluster. It confirms that cementite dissolves into the austenite phase as stated by several authors.[30–33]

C. *Carbon Concentration Profiles*

The carbon concentration profiles of the samples before and after annealing were measured by means of GD-OES as shown in Figure 9 for the steel coiled at 873 K (600 °C) (uniform microstructure) and annealed at 973 K (700 °C) for 200 seconds. The high values of carbon intensity at a few micrometers from the surface in the GD-OES depth profiles are due to impurities adsorbed at the surface.[34]

According to Figure 9(a), the material has been previously decarburized during the initial annealing. This decarburization may be due to exposure to the humidity present in the air during the homogenizing treatment at 1523 K (1250 °C) and the subsequent hot-rolling steps. The analysis of the carbon depth profile after annealing shows a near-surface region of about 35 μm thick with carbon concentration of no more than 200 ppm, which matches the maximum carbon solubility in ferrite. Therefore, this is interpreted as a carbide-poor ferrite layer. Going toward the bulk, the concentration of carbon gradually increases above the limit of carbon solubility in ferrite suggesting the presence of carbides, as observed in the microstructure of Figure 9(b). The density of carbides increases progressively until it reaches the bulk concentration.

In Figure 10 the effect of the decarburization temperature is studied on the basis of the carbon depth profiles obtained by GD-OES. As previously explained, austenite is not formed during annealing below the intercritical region and the microstructure at the end of the isothermal step consists of ferrite and cementite. The annealing at 973 K (700 °C) creates a significant ferrite layer of about 35 μm. The smooth increase of carbon concentration between the ferrite layer and the bulk concentration represents the presence of partially dissolved cementite.

In the case of isothermal holding just above the intercritical region, at 1023 K (750 °C), the carbon increase between the ferrite layer and the bulk concentration is more accentuated. The reason is that austenite is formed around cementite particles, which grows and merges with the neighboring austenite grains. The kinetics of austenite growth is limited at this temperature and its equilibrium fraction with ferrite is very small. It creates a region with partially dissolved cementite particles surrounded by thin layers of austenite isolated of each other just beneath the ferrite layer.

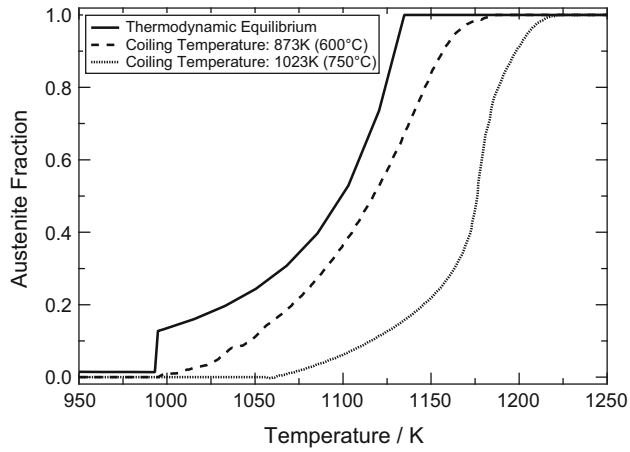

Fig. 7—Effect of the coiling temperature on the kinetics of austenite formation under constant heating rate of 25 K/s. The theoretical curve were obtained by ThermoCalc and the experimental values by dilatometry.

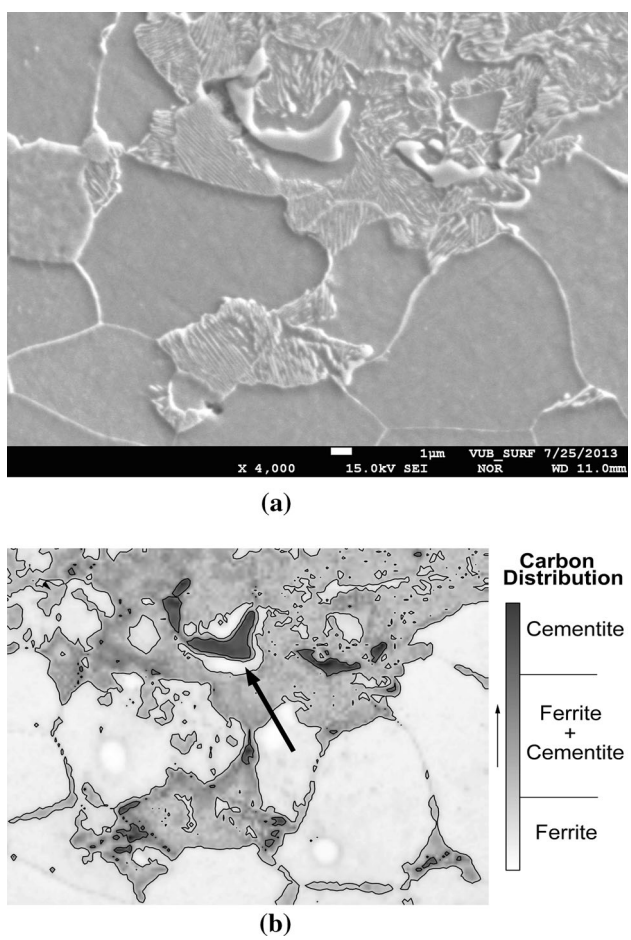

Fig. 8—Carbon distribution in the microstructure after annealing at 1023 K (750 °C) for 200 s. A partially dissolved cementite particle is surrounded by a pearlitic formation. During annealing the cementite particle is dissolved into austenite from which pearlitic structures are generated after cooling. (*a*) SEM image, (*b*) FE-EPMA-WDS.

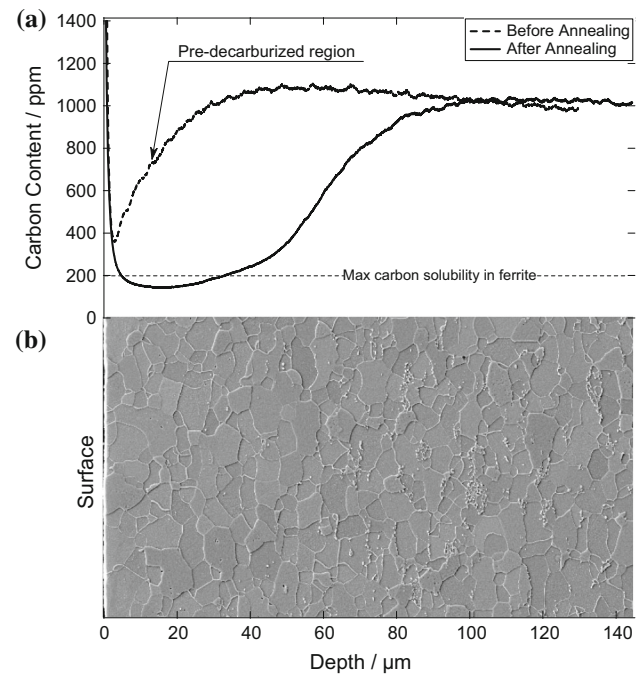

Fig. 9—(*a*) Carbon depth profiles obtained by GD-OES before and after annealing at 973 K (700 °C) for 200 s compared with (*b*) FE-SEM microscopy showing the distribution of cementite.

At 1083 K (810 °C) and above the carbides are completely dissolved at the end of the isothermal step and the end of the ferrite layer is characterized by a relatively sharp increase of carbon concentration. As the carbon solubilities are very distinct between ferrite and austenite, in the presence of a decarburizing atmosphere austenite is present in the bulk and ferrite near the surface. The sharp carbon concentration increase is interpreted as the probable position of the α/γ interface, denoted as ξ in Figure 10.

The concentrations in the depth profiles are in fact the average carbon concentration over an area of 50 μm^2 at a given depth, therefore, the α/γ interface is not sharp but it spreads over a small range of depth. Beyond the interface the carbon concentration increases gradually to the bulk composition representing the carbon diffusion in austenite phase.

With the increase of the annealing temperature to 1153 K (880 °C), the interface step is reduced because the austenite is now stable at smaller carbon concentration and the carbon diffusion in austenite is more pronounced. The ferrite layer is smaller due to the smaller formation of austenite at lower carbon concentration.

After annealing at 1193 K (920 °C) two regions are observed concerning the carbon concentration: a region with a concentration gradient and a region with constant concentration near the surface. Austenite is the only phase present. The region where the gradient exists, carbon diffuses from the bulk toward the surface. The region with the constant carbon concentration is originated from the ferrite layer generated during heating under decarburizing atmosphere. The austenite phase

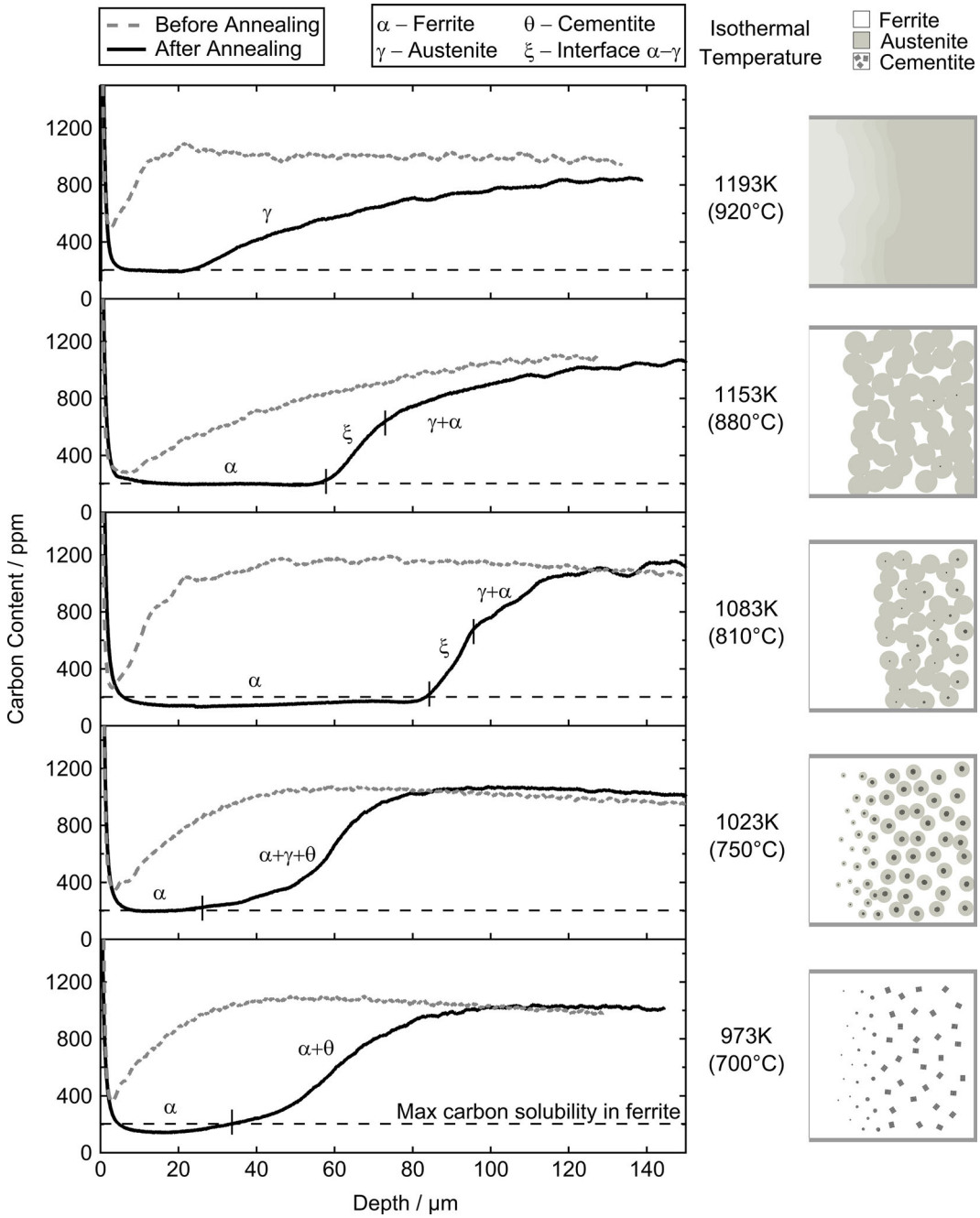

Fig. 10—Evolution of the carbon depth profile as a function of the annealing temperature for 200 s for the material coiled at 873 K (600 °C). The positions of the transitions between the regions are indicative.

grows from the bulk toward the surface. During the isothermal holding the carbon diffuses accordingly to reduce the concentration step at around 25 μm. After sufficiently long isothermal holding the concentration step is expected to be no longer present.

Due to the complexity of the mechanism of decarburization and the determination of its depth, a common approach is the measurement of the width of the ferrite layer as it is very simple to visualize and quantify this region.[15,35,36]

In Figure 11 an overview of the ferrite layer thickness as a function of the isothermal temperature and time is presented. The plot is based on the carbon depth profiles obtained by GD-OES. In case of the presence of a pre-decarburized layer, the difference in ferrite width before and after annealing is taken. A contour plot was created from the measurements shown in Figure 11(a) and plotted in Figure 11(b). It gives an overview of the width of the ferrite layer as a function of the isothermal parameters of temperature and time.

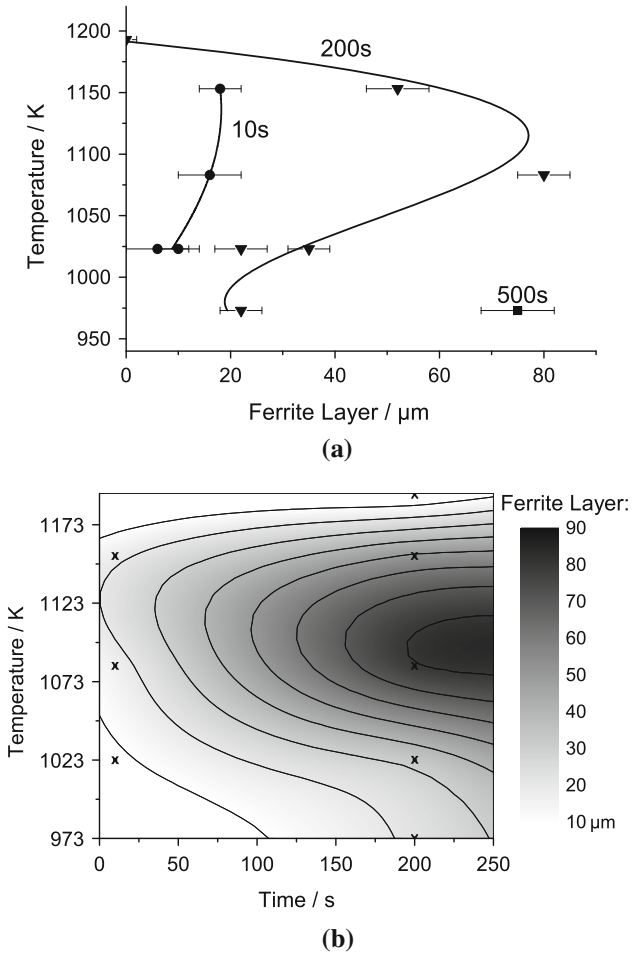

Fig. 11—Overview of the thickness of the ferrite layer as a function of the temperature for samples coiled at 873 K (600 °C). (*a*) Experimental results of the thickness of the ferrite layer under annealing at different temperature and time. The solid curve is a guide to the eye. (*b*) Contour plot of the experimental values illustrating the overall behavior of the thickness of the ferrite layer as afunction of the annealing conditions.

The temperature can affect decarburization in two ways. First, the dissolution rate of cementite and the diffusivity in both phases (austenite and ferrite) increases with temperature, contributing to a thicker ferrite layer after a given time. Second, the austenite fraction increases with temperature. Since carbon diffuses slower in austenite than in ferrite and it is more soluble in austenite, the presence of austenite reduces the thickness of the ferrite layer as a consequence of slower decarburization kinetics. Owing to these opposite effects, a temperature of maximum decarburization rate exists.

D. *Effect of the Cementite Distribution on Decarburization*

In Figure 12, the effect of the cementite distribution on decarburization is presented. As shown in Figure 3(a), the coiling temperature changes the morphology of the carbides before annealing. The coiling temperature of 873 K (600 °C) generates a microstructure composed of carbides distributed in the form of pearlite colonies that are evenly spread between the grains of ferrite. The carbon concentration profiles in Figure 12 on the left show a very uniform concentration over the GD-OES measurement area. The coiling at 1023 K (750 °C) generates very coarse carbides segregated over the microstructure, precipitated on the grain boundaries as shown in Figure 3(b). The concentration profiles in Figure 12 on the right show considerable variation of carbon concentration over the thickness, demonstrating coarse carbides distributed through the matrix.

The thickness difference of the ferrite layer before and after annealing at 1023 K (750 °C) is similar for both microstructures. At this temperature, the kinetics of austenitization is not very high and only a small fraction of austenite is formed around the carbides. The presence of a small fraction of austenite does not significantly affect the carbon distribution after the decarburization annealing for the two different materials. Consequently, the thickness of the ferrite layer formed is similar for both materials.

After annealing at 1083 K (810 °C) the carbon concentration profiles are very different. The presence of coarse cementite particles in the material coiled at 1023 K (750 °C) causes much smaller decarburized regions to be present than in the material having small pearlitic colonies prior to annealing. The presence of coarse particles reduces the kinetics of carbide dissolution and creates large austenite regions around the particles as observed in Figure 6(b). The formation of austenite is limited by the available surface area of the carbides, inducing a lower austenitization rate for coarse carbides as shown in Figure 7. Additionally, the higher carbon solubility and lower diffusivity for carbon in austenite slows down the overall diffusion of carbon through the material toward the surface, where carbon is removed. On pearlitic colonies, a greater surface area available for carbide dissolution into austenite is present, leading to a higher dissolution rate. As the concentration of carbon in the pearlitic colonies is lower than in coarse cementite particles, the austenite regions formed around the pearlitic colonies are also smaller but more numerous through the material, leading to a more homogeneous carbon distribution.

At 1153 K (880 °C) the austenite fraction is increased, reducing the ferrite layer beneath the surface in the material having pearlite colonies prior to annealing. The material coiled at 1023 K (750 °C) is heavily decarburized prior to annealing. During annealing, the carbides are dissolved into large austenite regions. At this temperature, austenite is stable at lower carbon concentration and it is formed near the surface. As the carbon is constantly removed from the surface during the isothermal treatment, the carbon in the bulk diffuses toward the surface to the newly formed austenite region, eventually increasing the initial carbon composition in the pre-decarburized region.

IV. CONCLUSIONS

It was observed that coiling temperature has a strong influence on the carbide morphology. Fine-pearlitic structures are found at low-coiling temperature and its

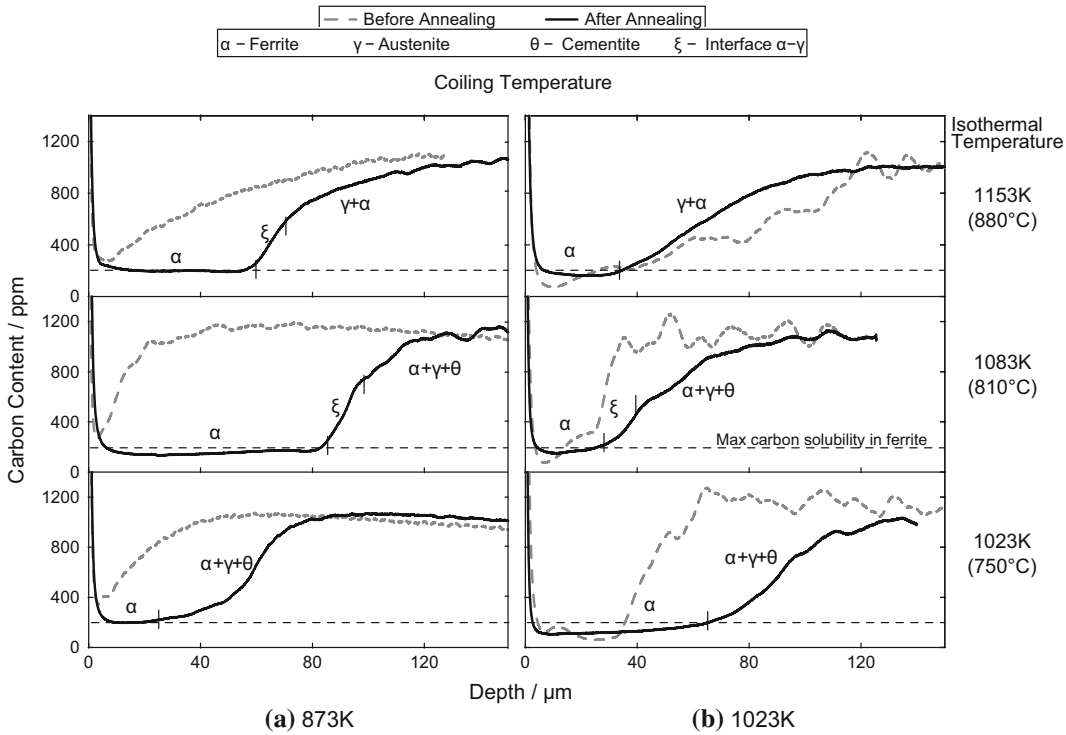

Fig. 12—Comparison of carbon depth profiles by GD-OES after annealing for samples with different coiling temperatures: 873 K (600 °C) on the left column and 1023 K (750 °C) on the right column.

coarseness increases with increasing coiling temperature. After coiling in the intercritical region, cementite particles unpaired with ferrite can be detected in the microstructure.

The initial microstructure having fine pearlite structures shows fast decarburization kinetics, particularly at higher temperatures, suggesting that austenite formation kinetics has a substantial effect on carbon mobility.

The width of the ferrite layer beneath the surface is a result of the combination of opposing effects of diffusion of carbon and the thermodynamic fraction of austenite at a given temperature. A maximum ferrite layer occurs in the intercritical region.

The dissolution of cementite influences the decarburization kinetics through the interference on the austenitization kinetics. Coarse carbides dissolve slowly due to their low surface area, thus retarding the decarburization kinetics.

REFERENCES

1. H. Grabke: *Metall. Trans. B*, 1970, vol. 1B, pp. 2972–75.
2. H. Grabke and G. Tauber: *Arch. Eisenhuttenwes.*, 1975, vol. 46, pp. 215–22.
3. D. Li, D. Anghelina, D. Burzic, J. Zamberger, R. Kienreich, H. Schifferl, W. Krieger, and E. Kozeschnik: *Steel Res. Int.*, 2009, vol. 80, pp. 298–303.
4. N. Birks and W. Jackson: *J. Iron Steel Inst.*, 1970, vol. 208, pp. 81–85.
5. C. Oldani: *Scripta Mater.*, 1996, vol. 35, pp. 1247–1371.
6. R. PremKumar, I. Samajdar, N. Viswanathan, V. Singal, and V. Seshadri: *J. Magn. Magn. Mater.*, 2003, vol. 264, pp. 75–85.
7. K. Marra, E. Alvarenga, and V. Buono: *ISIJ Int.*, 2004, vol. 44, pp. 618–22.
8. Y. Kim and H. Leckie: *Metall. Trans. B*, 1975, vol. 6, pp. 303–10.
9. H. Grabke: *Arch. Eisenhuttenwes.*, 1975, vol. 46, pp. 75–81.
10. B. Korousic and B. Stupnisek: *Kovine Zlitine Tehnol. (Slovenia)*, 1996, vol. 30, pp. 521–26.
11. B. Soenen, S. Jacobs, and M. De Wulf: *Steel Res. Int.*, 2005, vol. 76, pp. 425–28.
12. R. Baggerly and R. Drollinger: *J. Mater. Eng. Perform.*, 1993, vol. 2, pp. 47–50.
13. A. Phillion, H. Zurob, C. Hutchinson, H. Guo, D. Malakhov, J. Nakano, and G. Purdy: *Metall. Mater. Trans. A*, 2004, vol. 35A, pp. 1237–42.
14. J. Gegner: *The Fourth International Conference on Mathematical Modeling and Computer Simulation of Materials Technologies*, 2006.
15. S. Choi and S.V.D. Zwaag: *ISIJ Int.*, 2012, vol. 52, pp. 549–58.
16. J. Verhoeven: *Mater. Charact.*, 1990, vol. 25, pp. 221–39.
17. M.A. Borodin: *J. Math. Sci.*, 2011, vol. 178, pp. 13–40.
18. D. Mercier, X. Decoopman, and D. Chicot: *Surf. Coat. Technol.*, 2008, vol. 202, pp. 3419–26.
19. O. Perevertov, O. Stupakov, I. Tomáš, and B. Skrbek: *NDT & E Int.*, 2011, vol. 44, pp. 490–94.
20. B. Sundman, B. Jansson, and J. Andersson: *CALPHAD*, 1985, vol. 9, pp. 153–90.
21. J. Zhao, C. Mesplont, and B. De Cooman: *Mater. Sci. Eng. A*, 2002, vol. 332, pp. 110–16.
22. A. Bengtson: *Spectrochim. Acta Part B At. Spectrosc.*, 1985, vol. 40, pp. 631–39.
23. T. Nelis, M. Aeberhard, R. Payling, J. Michler, and P. Chapon: *J. Anal. At. Spectrom.*, 2004, vol. 19, pp. 1354–60.
24. A. Bengtson: *Spectrochim. Acta Part B At. Spectrosc.*, 1994, vol. 49, pp. 411–29.
25. R. Payling, D.G. Jones, and S.A. Gower: *Surf. Interface Anal.*, 1995, vol. 23, pp. 1–11.
26. B. Panigrahi: *Bull. Mater. Sci.*, 2001, vol. 24, pp. 361–71.
27. A. Van Cauter, J. Dilewijns, F. Hörzenberger, R. Hubert, and B. De Cooman: *J. Mater. Eng. Perform.*, 2000, vol. 9, pp. 131–37.
28. A. Pandit and H. Bhadeshia: *Proc. R. Soc. A Math. Phys. Eng. Sci.*, 2012, vol. 468, pp. 2767–78.

29. J. Verhoeven and E. Gibson: *Metall. Mater. Trans. A*, 1998, vol. 29A, pp. 1181–89.
30. G. Speich, V. Demarest, and R. Miller: *Metall. Trans. A*, 1981, vol. 12A, pp. 1419–28.
31. C. Garcia and A. DeArdo: *Metall. Trans. A*, 1981, vol. 12, pp. 521–30.
32. D. Shtansky, K. Nakai, and Y. Ohmori: *Acta Mater.*, 1999, vol. 47, pp. 2619–32.
33. D. Gaude-Fugarolas and H. Bhadeshia: *J. Mater. Sci.*, 2003, vol. 38, pp. 1195–1201.
34. I. Calliari, M. Dabalà, E. Ramous, M. Zanesco, and E. Gianotti: *J. Mater. Eng. Perform.*, 2006, vol. 15, pp. 693–98.
35. C.-L. Zhang, Y.-Z. Liu, L.-Y. Zhou, C. Jiang, and J.-F. Xiao: *Int. J. Miner. Metall. Mater.*, 2012, vol. 19, pp. 116–21.
36. J. Snoek: *Physica*, 1941, vol. 8, pp. 734–44.